

OPTIMAL TRUSS-TYPE SUPPORTS FOR MINIMAL PART DISTORTION IN LPBF

Subodh C. Subedi^{*1}, Dan J. Thoma^{1,2}, and Krishnan Suresh¹

¹Mechanical Engineering Department, University of Wisconsin-Madison, USA

²Material Science and Engineering Department, University of Wisconsin-Madison, USA

Abstract

Efficient transfer of heat to the build plate is important for part printability in laser powder bed fusion (LPBF). Support structures provide pathways for heat dissipation from the melt pool to the build plate. Truss-type supports have been proposed for better thermal management in LPBF since they are easy to analyze, optimize and post-process. In this paper, we consider thermo-elastic LBPF simulations, where a part and corresponding truss-type support are progressively coupled during the build process. Transient thermal FEA is performed as each layer is built to obtain temperature profiles. Thermal and structural equivalent static loads are obtained from the transient results, which are accumulated to compute aggregate structural equivalent static loads (ASESL). Structural deformation of coupled systems involving part and truss-type supports is also computed after each layer-wise built. Finally, cross-sectional areas of truss-type supports are optimized using ASESL to minimize structural deformation. Optimized supports show a significant reduction in part deformation compared to un-optimized supports. Numerical results are presented to demonstrate the merits of the proposed method.

Introduction

Powder-based metal additive manufacturing (AM) is one of the most advanced manufacturing processes today. The use of 15 to $45\mu\text{m}$ metal powders and 50 to $100\mu\text{m}$ sized laser beams makes them the preferred choice for parts with small features and high accuracy requirements. With the advancements in material, part, and process designs, the technology has enabled manufacturing of numerous functional components ranging in applications from aerospace [1, 2], automobile [3], biomedical [4, 5] to electronics [6] and many more.

Laser powder bed fusion (LPBF) processes suffer from very high thermal stresses due to expansion and contraction during rapid heating and cooling cycles [7, 8]. These stresses

*Corresponding email: scsubedi@wisc.edu

lead to part distortion [9] and can even damage the machine due to recoater collision. Part distortion and residual stresses have been the major bottlenecks in the wider adoption of LPBF technology. A better understanding of the mechanism for such failure and appropriate solutions to address them are of greater need. Three major categories of parameters that govern the success of part printing in LBPF are:

1. Material parameters: These are material-dependent parameters. They define the shape and size of metal powder, thermal conductivity, density, absorptivity, reflectivity, surface tension, wetting angle, melt viscosity, flowability, etc.
2. Process parameters: These are the parameters related to the printing process. These include laser speed, laser size, laser power, layer thickness, platform temperature, scan patterns, recoater travel speed, gas flow rate, etc.
3. Geometry parameters: These are the part geometry-related parameters such as threshold overhang angle, minimum feature size, part aspect ratio, build orientation, minimum build height, support structures, etc.

Material parameters and process parameters primarily dictate the micro-structural and mechanical properties of the part being printed [8, 10, 11, 12, 13, 14]. Part geometries also affect the thermal history of any part built and influence the microstructural properties, but, the geometric parameters mostly act on determining dimensional accuracy, part printing and post-processing time and costs. Numerous efforts have been carried out targeting the minimization of build time and costs by identifying optimized build configurations [15, 16, 17, 18, 19]. Part-build configuration involves part placement above the build platform and its orientation in the build chamber. Further, part printability based on feature sizes was quantified by Bracken et al. [20] for powder bed fusion based AM.

Support structures for part printability remain an active area of research. Support structures are the sacrificial components in LPBF that are added between the build plate and the part to prevent structural damage to the part during post-processing removal. Supports in LPBF are primarily thermal supports, that act as pathways for rapid heat dissipation from the melt pool to the build plate. Support structures are also known to influence the microstructural properties within a part [21, 22, 23]. Well-designed supports have demonstrated reduced build failures by minimizing part deformations [14, 24, 25].

This paper demonstrates the use of one type of supports in minimizing part deformations. Specifically, truss-type supports are generated based on the threshold overhang angles and ray tracing. Transient thermal analysis of coupled parts and supports is carried out to compute temperature distribution within the part and support. The temperature solutions are used to find thermal and structural equivalent static loads. Aggregated structural equivalent static loads (ASESL) is then used to optimize the cross-section areas of truss-type supports. Comparative results for the maximum deformation of part and support between unoptimized and optimized supports demonstrate the advantages of optimization in controlling part deformation.

Part Deformation in LPBF

As a high-power laser melts a small section of powder over a relatively colder build plate, thermal gradients ($20\text{K}/\mu\text{m}$) are induced in the part [26]. The heated section expands with a convex upward profile, thereby protruding the central region out of the plane. Once the deposited layer begins cooling with a very high cooling rate (10^6K/s), a concave outward profile is generated, bending the edges of the layer [9, 27]. The geometry and process parameters are critical in controlling the out-of-tolerance deformation of layers due to cyclic loading and unloading of the heat input. As the LPBF process shares a lot of commonality with the welding process, out-of-plane part deformation can also be categorized as defined for weldments by Masubuchi [28, 29].

- Longitudinal Bending: The uneven shrinkage of solidified layer causing it to bend out of plane leads to longitudinal bending.
- Buckling: Buckling of thin solidified layer occurs when residual stress exceeds the critical buckling strength.
- Angular deformation: Transverse shrinkage of layer relative to the laser traverse direction is defined as angular deformation.

Longitudinal deformation are a major concern. Buckling and angular deformation are less evident in LPBF, due to relatively thicker build plates [29]. There are multiple different strategies aimed at minimizing part deformation.

1. Geometry Compensation: Possible part are obtained through physical and numerical experiments and geometric compensations are added into the part design itself to obtain higher geometric accuracy. Biegler et al. [30] used transient simulations to predict part deformations in directed energy deposition (DED), which were then inverted to modify the part geometry for minimizing deformations. Structural FE predicted deformations were compensated in initial geometry by inverting the displacement of nodal coordinates by Afazov et al. [31, 32]. They also proposed the use of optical 3D scans to construct a distorted CAD model of a printed part and then calculate the deformations of parts to incorporate in the initial model. Zhang et al. [33] modified the initial CAD geometry to include geometric compensation obtained from thermal deformation of a part modeled using NURBS.
2. Configure Geometric Features and Part Orientations: LPBF processes are widely used for their capabilities to print complex geometric features with greater accuracy, however, machine precision puts limits on the level of complexities in any part. Geometric features such as very high aspect ratio, small round holes, sharp edges, bridge gaps, etc, are important in part printing. Guidelines for part orientation and feature sizes have been proposed through multiple physical experiments to obtain better geometric accuracy. Adam and Zimmer [34] proposed geometry based design rules for laser sintering, laser melting and fused deposition modeling. Bracken et al. [20] designed a

worksheet to compute ratings of parts based on their geometric features that indicate the suitability of metal powder bed fusion process for the part.

3. Modify process parameters: Printing process parameters play a vital role in print success. A combination of scan powder, scan speed, and spot sizes was obtained by Huo et al. [35] for minimal part deformation. Mukherjee et al. [36] investigated the effect of laser power, scanning speed, layer height in thermal deformation of part. Reducing inter-layer dwell times minimized the accumulations of layer-wise deformation during part printing for titanium and nickel alloys [9]. Change in laser scan patterns also mitigates part deformation [7, 37]. Denlinger [29] proposed different methods involving additional material deposition to minimize part deformation in electron beam deposition by balancing the bending moment. Preheating the build plate to a higher temperature has also been conducive to reducing deformation [38].
4. Support structures: Support structures are added for efficient transfer of heat from the downward-facing overhang surfaces to the nearest build surfaces. Xie et al. [39] showed that part deformations are heavily influenced by the structural stiffness of support structures, as deformations for parts with support of higher shear stiffness had minimal deformations. Mishurova et al. [24] have shown that parts built on a solid bulk substrate have lower deformation compared to that over a support structure. However, use of such a bulk substrate adds more time, material, and costs to the printing process. Thus, there is a need for better support structure design that can potentially minimize part deformations and material usage.

This paper puts forward the idea of minimizing part deformation using support structures. The next section presents the support structure generation, analysis, and optimization strategies.

Truss-type support structures

Truss-type supports [40] are generated for downward-facing overhang surfaces. These are open structured designs that do not entrap any metal powders and are much easier to remove during post-processing. The algorithm proposed here improves upon the truss-type support structures by the authors [40]. Specifically, the algorithm proposed in [40] could only handle part-to-build support. Here, it is extended to handle part-to-part support as well by relying on ray-tracing [41].

Design

The 2D version of the algorithm is illustrated in Figure 1. A vertex of a triangle from an overhang surface is offset along the negative build direction to generate a projected point. Lines connecting the projected point with the rest of the overhang vertices that satisfy the self-support constraint are retained as truss members. The process repeats until all of the overhang vertices are supported by projected points. The projected points are then marked as overhang vertices. Ray-tracing is carried out from these overhang vertices to find the

nearest build surface. The next set of projected points are then generated. If the nearest build surface is closer than the distance to the next virtual layer, the projected point is moved to the build surface and marked as supported. The process of ray tracing, generating projected points, edge creation, and retention is repeated until all points are supported. This algorithm generates truss support for both part-to-part and part-to-build.

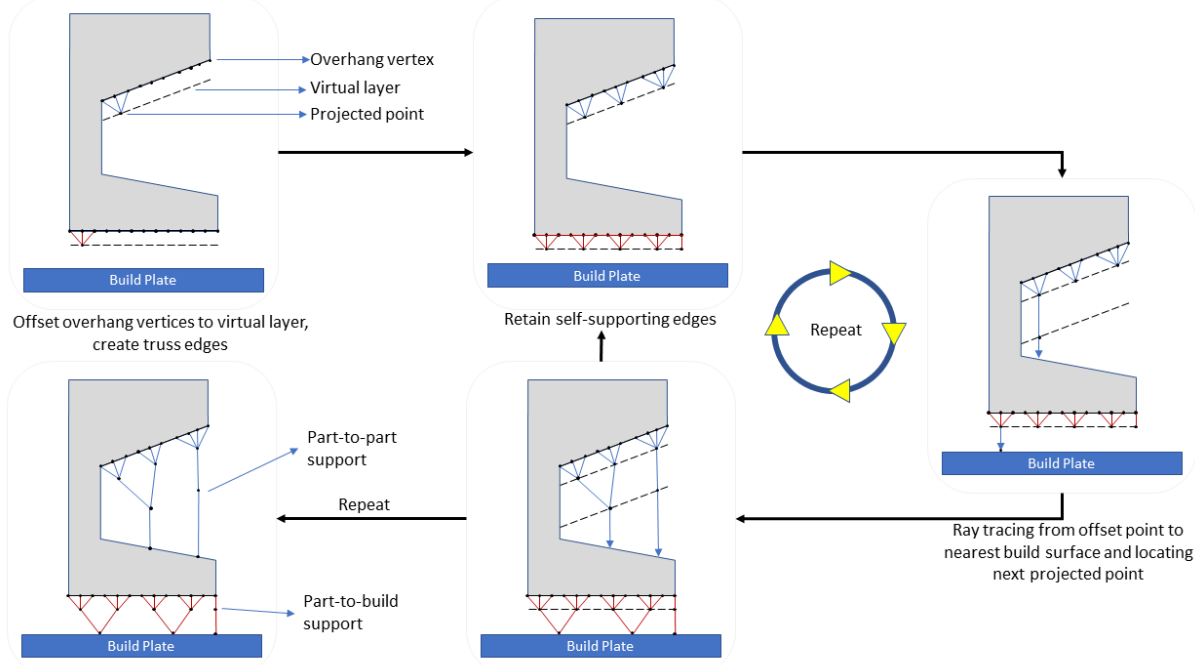


Figure 1: *Truss-type support generation using ray tracing*

Analysis

The analysis is performed on a coupled part-and-truss system. A part is first meshed using uniform hexahedral elements. These type of elements make it easier to simulate layer-wise part built as they resemble thick powder layers. The height of these elements is set to 25 times the powder layer height used in LPBF. Mesh convergence studies using similar mesh sizes have shown to have minor effects in the maximum temperature variations [42]. Use of finer mesh elements would generate results with higher accuracy but at significant computational costs. Thus, 25 physical layers are combined to form a mesh layer for a balance of accuracy and efficiency.

Each of the exposed truss nodes is coupled to hexagonal elements based on their proximity as illustrated in Figure 2. Active coupled systems are constructed by trimming the truss-type support and the hex-meshed part based on layer height. The active systems evolve as the part build height increases based on the mesh layer being built. Examples in Figure 3 illustrate the idea of evolving coupled systems or active systems. Active system 1, shown in Figure 3a, is constructed by trimming the hex-meshed part and the truss-type support with the layer height being 1 hex-mesh element size. Other active systems are also constructed

in a similar way.

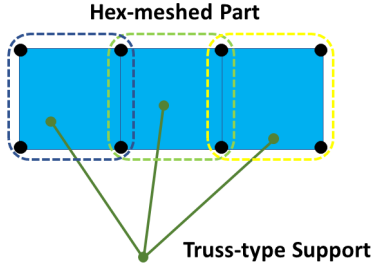


Figure 2: Truss node to hex-element coupling.

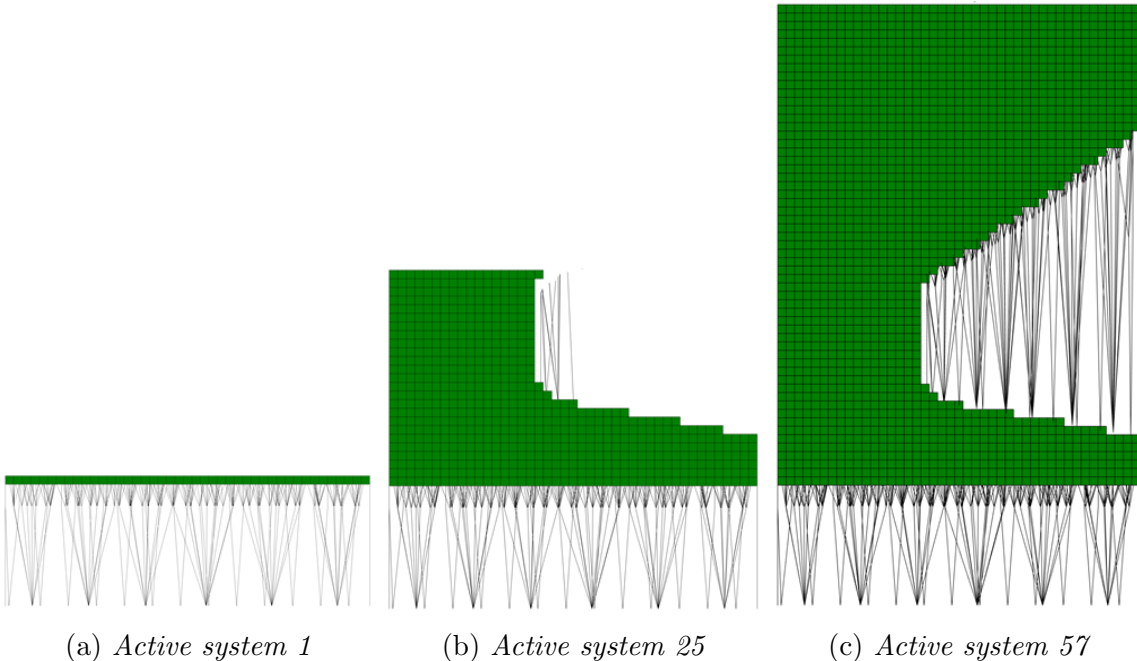


Figure 3: Active systems based on the hex-mesh layers.

Transient thermal finite element analysis is performed over the active coupled systems, simulating the layer-wise build process. For carrying out the FE analysis, coupled systems are assembled as in Equation 1, where K_{hex} and K_{truss} are the thermal stiffness matrices for active hex elements and the truss-type supports. M_{hex} and M_{truss} are the thermal mass matrices for active hex elements and truss-type supports. C^T is a constraint matrix whose components are derived from the tri-linear shape functions of the hexagonal elements (see Figure 2).

$$K_{coupled} = \begin{bmatrix} K_{hex} & 0 & C^T \\ 0 & K_{truss} & 0 \\ C & 0 & 0 \end{bmatrix}, M_{coupled} = \begin{bmatrix} M_{hex} & 0 & C^T \\ 0 & M_{truss} & 0 \\ C & 0 & 0 \end{bmatrix} \quad (1)$$

During the transient thermal analysis, the chamber temperature is assigned as the initial temperature to all the truss and hex-meshed parts. A dirichlet boundary condition with

fixed temperature of 80°C is assigned to the nodes in contact with the build plate. Heat flux (F_a) is applied to all the nodes on the current top-most layer of the part. The heat flux is computed using the number of elements, laser parameters and absorptivity of the material powder [43, 44] as follows:

$$VED = \alpha \frac{P}{vh_t h_s} \quad (2)$$

$$F_a = \frac{VED}{Nt_s} V_L \quad (3)$$

where, VED is volumetric energy density, α is the laser absorptivity, P is the laser power, v is the laser scan speed, h_t is the powder layer height, and h_s is the hatch spacing. V_L is the volume of material, N is the number of nodes on the top-most layer of active coupled system. t_s is the time required to scan the topmost layer of the active system computed using laser speed, hatch spacing and layer surface area.

Time stepping for transient thermal analysis is carried out using the Newmark-Beta scheme [45, 46]:

$$[K_{eff}]\{T_{n+1}\} = \{F_{eff}\}_{n+1} \quad (4)$$

where, K_{eff} and F_{eff} are the effective global stiffness matrix and force vectors given by

$$[K_{eff}] = \frac{1}{\Delta t} [M_{coupled}] + [K_{coupled}] \quad (5)$$

$$\{F_{eff}\}_{n+1} = \frac{[M_{coupled}]}{\Delta t} \{T_n\} + \{F\}_{n+1} \quad (6)$$

and,

$$T = \begin{bmatrix} T_{hex} \\ T_{truss} \\ \lambda \end{bmatrix} \quad (7)$$

where λ 's are the Lagrange multipliers.

Two stages of finite element analyses are carried out. The first FE analysis is performed at the end of time $\Delta t = t_s$ with $F = F_a$. Temperature values obtained from the first FE are used as initial values for the second FE analysis carried out with time $\Delta t = t_r$ and $F = 0$, where t_r is the recoater travel time to lay a new layer of powder. The second round of FE incorporates the time-dependent heat dissipation of the active systems during recoater travel when the laser is turned off. Results from the second FE analysis are used as initial temperatures for the next layer build, and the process continues until the part build simulation is complete. Thermal equivalent static loads (ESL) is computed using results of each of the transient finite element analyses. ESL is defined as the static thermal load that would generate the same temperature solutions as that by the transient thermal analysis [42] carried out here, and is computed as follows:

$$\{f_{ESL}\} = [K_{truss}]\{T_{truss}\} \quad (8)$$

Then, the structural equivalent static load (SESL) is denoted by H and can be computed from ESL based on the formulation proposed by Deng and Suresh [47].

$$[H]\{\Delta T\} = \{f_{ESL}\} \quad (9)$$

where,

$$[H] = \sum_{e=1}^{Num} \left(\int_{\Omega_e} B_e^T D_e \alpha \Phi^T d\Omega \right) \quad (10)$$

$$\{\Delta T\} = T_{truss} - T_{chamber}$$

where, B_e is the element strain-displacement matrix, D_e is the element elasticity matrix, α is the coefficient of thermal expansion, Φ is $[1 \ 1 \ 1 \ 0 \ 0 \ 0]$ vector in 3D, Num is the number of elements in an active system and $T_{chamber}$ is the build chamber temperature.

The structural equivalent static load H , is used to obtain the structural deformation of both the part and supports at the end of each layer-wise build simulation using Equation 9, and 10. A static structural FEA engine is used to compute the structural deformation of parts using SESL. The truss nodes connected to build surfaces are assigned a fixed boundary condition while SESL is applied at each of the other nodes. The truss members are assigned a surface-based 4-finned shape [40, 42], along with a uniform area in the cross-section.

Aggregate structural equivalent static load (ASESL) on the truss-type support is computed using the individual equivalent static structural load vectors as is computed for aggregate equivalent static loads by the authors [42]. ASESL takes the maximum values of SESL at each of the truss nodes obtained from the results of all active system FE analyses. This provides the maximum structural load each truss node has to bear during the entire part-built process. ASESL is defined as:

$$\{H_{ASESL}\} = \max(\{H_{ASESL}^a\}) \quad (11)$$

where, a varies from 1 to the total number of layers.

Optimization

The aggregate structural equivalent static load (ASESL) computed from the layer-wise build simulations is now used to optimize the cross-section area of the truss-type supports. ASESL and structural deformation solutions corresponding to the truss-type support are extracted as H_{ASESL} and d_{truss} respectively. The optimization formulation involves minimization of structural compliance subjected to a volume constraint and is stated as shown in Equation 12.

$$\begin{aligned}
\min_{\{a_i\}} \quad & J = \{H_{ASESL}^T\}\{d_{truss}\} \\
\text{s.t.} \quad & [K_{truss}]\{d_{truss}\} = \{H_{AESL}\} \\
& h = \sum_{e=1}^m \frac{A_e l_e}{V^*} - 1 \leq 0 \\
& A_e^{min} \leq A_e \leq A_e^{max}
\end{aligned} \tag{12}$$

where, J is the structural compliance, A_e and l_e are the area and lengths of truss elements. V^* is the limit of support volume, whereas A_e^{min} and A_e^{max} are the limits on individual truss areas based on their manufacturability. The d_{truss} vector contains the nodal deformations obtained from FEA.

The truss area optimization is carried out using GCMMA [48]. The optimizer requires objective value, constraint value and their sensitivities towards the areas. The sensitivity of the objective (structural compliance) is computed using the following formulation,

$$\begin{aligned}
J &= H_{ASESL}^T\{d_{truss}\} \\
\frac{\partial J}{\partial A_e} &= ([K_{truss}]\{d_{truss}\}) \frac{\partial\{d_{truss}\}}{\partial A_e}
\end{aligned} \tag{13}$$

Differentiating the state equation, $[K_{truss}]\{d_{truss}\} = \{H_{AESL}\}$, with respect to the cross-section area, we have,

$$\begin{aligned}
\frac{\partial[K_{truss}]}{\partial A_e}\{d_{truss}\} + [K_{truss}] \frac{\partial\{d_{truss}\}}{\partial A_e} &= 0 \\
[K_{truss}] \frac{\partial\{d_{truss}\}}{\partial A_e} &= -\frac{\partial[K_{truss}]}{\partial A_e}\{d_{truss}\}
\end{aligned} \tag{14}$$

From Equation 13 and 14, we get,

$$\begin{aligned}
\frac{\partial J}{\partial A_e} &= -\{d_{truss}^T\} \frac{\partial[K_{truss}]}{\partial A_e}\{d_{truss}\} \\
\frac{\partial J}{\partial A_e} &= -d_e^T \begin{bmatrix} 1 & -1 \\ -1 & 1 \end{bmatrix} d_e \frac{E}{l_e}
\end{aligned} \tag{15}$$

where, d_e are the nodal displacements of the two nodes of each of the truss elements and E is the young's modulus of elasticity for the material in use.

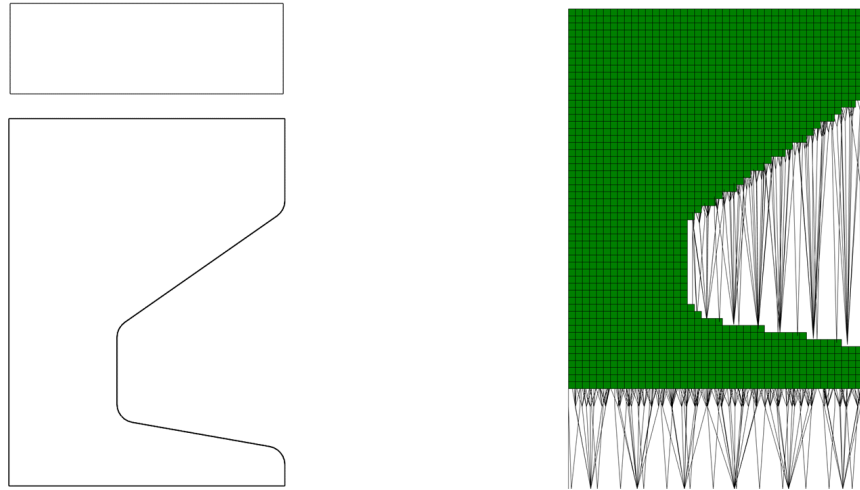
Similarly, the sensitivity of the constraint (volume) is given by,

$$\frac{\partial h}{\partial A_e} = \frac{l_e}{V^*} \tag{16}$$

The objective, constraint, and their corresponding sensitivities against the cross-section areas are appropriately scaled to avoid numerical issues. The truss area optimization results in the optimal distribution of material on the truss members for better structural strength management within the support domain. The optimized area values are assigned to the truss members and the layer-wise build is simulated again to compute ESL, SESL. A comparative analysis of relative deformations of parts from every layer-wise built simulation indicates a reduction in deformation for a part built over optimized truss-type support.

Numerical Experiment

A specimen with different types of overhang surfaces is chosen for numerical experiments. The specimen has one downward facing overhang surface inclined at 55° with the build direction and the other is flat. Two different views of *Part 1* are shown in Figures 4a respectively.



(a) *Part 1* specimen: Top and Front Views (b) Hex-meshed *Part 1* with truss-type support

Figure 4: Specimens details with corresponding truss-type supports.

Truss-type supports are generated as discussed earlier for both the overhang surfaces. The minimum support height is taken to be 5mm about the build plate for ease of analysis and post-processing removal. The part is hex meshed and coupled with its corresponding truss-type support based on node-to-element proximity as seen in Figure 4b. Active coupled systems are created by trimming the truss-type support and hex-meshed part. Heat flux computed using Equation 3 is applied on the nodes of the topmost layer of the active system. Temperature solutions from transient thermal FEA are used to obtain ESL and SESL for the part and the truss.

Results and Discussion

Active systems for the specimen are solved using transient thermal FEA engines. Results for transient temperatures at different instances are shown in Figure 5. Maximum temperature values in these active systems are extracted after each round of FEA. The variations

in maximum temperatures during layer-wise built simulations for hex-meshed *Part 1* and corresponding truss-type supports are shown in Figures 6 and 7 respectively.

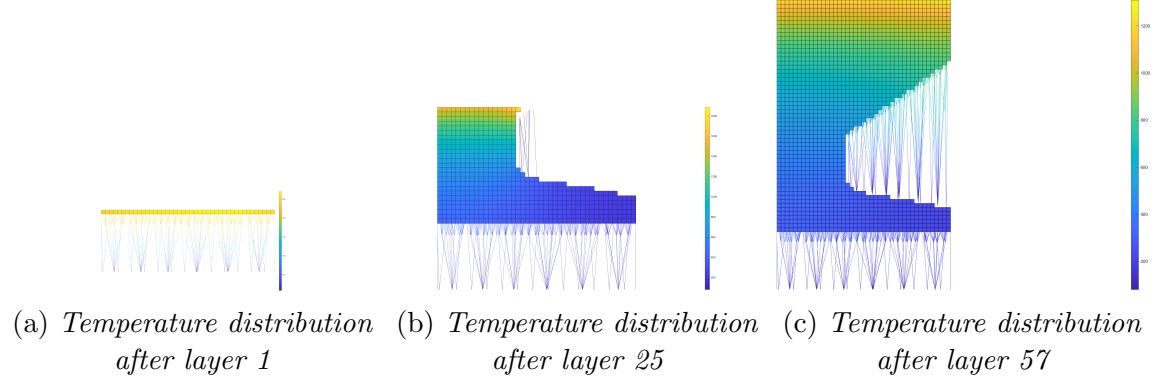


Figure 5: *Temperature distributions in active systems.*

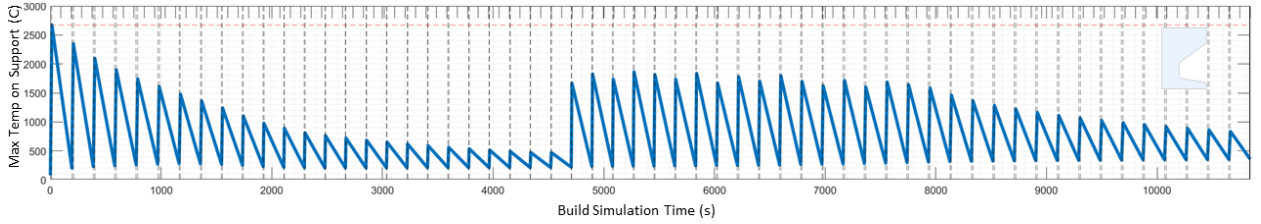


Figure 6: *Maximum temperature variation in truss-type supports for Part1 specimen*

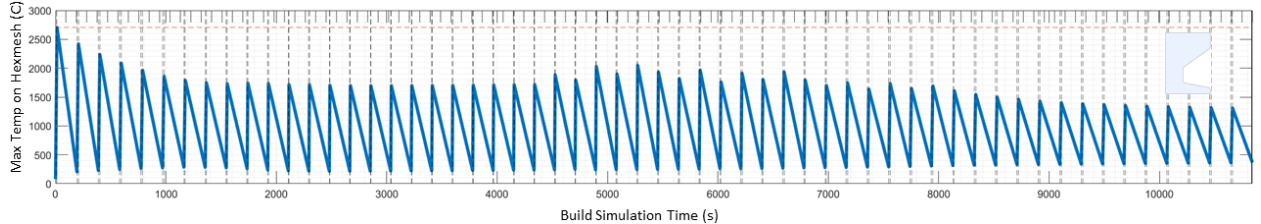


Figure 7: *Maximum temperature variation in hex-meshed part for Part1 specimen*

The temperature variations show a serrated pattern for the two FEA runs carried out at each layer. The peaks indicate the results from the first transient thermal FEA where the laser is turned on for the duration of laser scan time(t_s), whereas the dip in temperature values indicates the point where the laser is turned off and heat is being rapidly dissipated to the build plate. The maximum temperature values on the truss-type supports gradually decline towards the middle of the plot as seen in Figure 6. As the supports are not directly loaded until the inclined surface built simulation begins, the maximum temperature in the truss keeps decreasing. Also much of the heat is accumulated in the hex-meshed part as the truss members are assumed to have very small area values, and do not store any energy. The rise in the maximum temperature values towards the middle of the plot for the support (see Figure 7) indicates the results from simulation of layers with inclined surfaces on *Part 1*, where the truss members are not in contact with the inclined overhang surface. For the

hex-meshed part, the maximum temperature values do not follow a similar trend as the nodes on the part are always applied a heat flux load, as seen in Figure 7.

The temperature values do not indicate the actual temperature for the part built as several assumptions and simplifications have been made for the analysis. The truss elements are assumed to only have longitudinal heat conduction as lateral heat dissipation has been neglected. Multiple physical layers have been combined to create a single mesh layer for faster and easier computation. Material properties have been assumed to be constant and have been referred to at room temperature. The objective of the paper is to show the change in relative part deformation by using optimized support structures, the relative distribution of thermal load is more of our interest than the exact values.

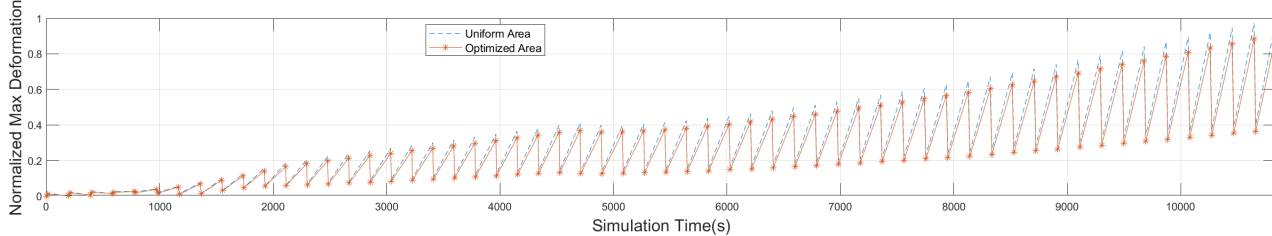
ASESL computed using Equation 11 is used to optimize the support structures. The support volumes of 21.15% has been used for the truss-type support as referred from Materialize Magics®. Once the support is optimized for minimum structural compliance, it is used for layer-wise build simulation again. A reduction of 40% structural compliance is obtained for the truss-type support after optimization. Equivalent static structural load is computed at the end of each transient thermal FEA and static structural FEA is carried out to compute deformation of the coupled system involving the hex-meshed part and the truss-type support.

Using the results of structural deformation computed from SESL, maximum values at each layer-wise simulation are obtained for cases with unoptimized and optimized truss-type supports. The values are normalized against the maximum deformation values and plotted against the simulation times. Comparative results for normalized deformation of part and supports for *Part 1* is shown in Figure 8.

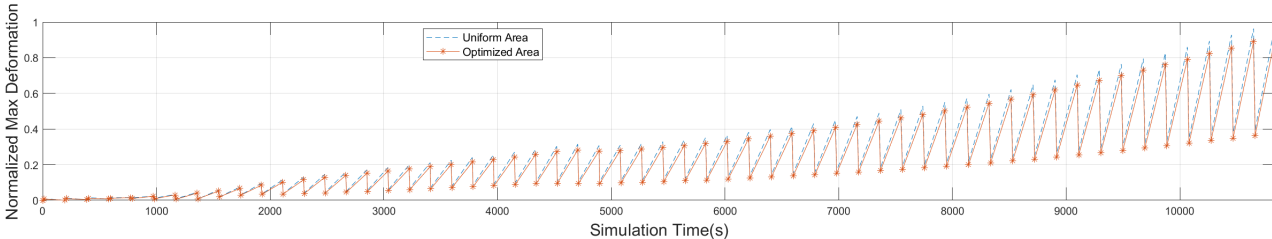
Results for the *Part 1* specimen indicate a reduction in part and truss-type support deformation between unoptimized and optimized supports. The reduction is greater for the supports compared to the parts when optimized supports are used. Though the structural deformation values do not differ significantly between unoptimized and optimized supports, it is still important to minimize part deformation, and support structure optimization can be one of the ways to do so. The minimal change is likely due to very small area values assigned to the truss-type support members. The thicknesses are close to the minimum manufacturable area for the given set of material and processing parameters. Also, as demonstrated earlier by the authors [40], truss-type supports use less than 20% material compared to the commonly used block-type supports, making a huge amount of material saving. Assigning more material to the truss-type supports will result in larger areas of the truss members that could yield better reduction in part and support deformations.

Conclusion

Part deformation is one of the biggest challenges in the LPBF process. This paper attempts at identifying the types of part deformations and the reasons behind them. Finally, one of the ways to control part deformations was presented in the paper. Numerical results indicated a reduction in maximum part deformation per layer when optimized supports were used. Part deformation can be minimized by providing optimal material distribution leading



(a) *Normalized deformation for truss-type support for Part 1 specimen*



(b) *Normalized deformation for hex-meshed part for Part 1 specimen*

Figure 8: *Normalized deformations for Part 1 specimen.*

to better load management within the supports. Numerous simplifications were made in the analysis and optimization of the supports, thus errors are inevitable. Linearity of material and the process are major sources of error. However, these simplifications led to faster and easier analysis of parts built with truss-type supports. The numerical results need to be validated through physical printing and measurement of parts, which will be carried out and presented in subsequent publications.

Acknowledgment

The authors would like to thank the generous support of NAVAIR and Technical Data Analysis Inc. for this work.

References

- [1] Andres Gasser, G Backes, I Kelbassa, A Weisheit, and K Wissenbach. Laser metal deposition (lmd) and selective laser melting (slm) in turbo-engine applications. *Laser Technik Journal*, 2:58–63, 2010.
- [2] Byron Blakey-Milner, Paul Gradl, Glen Snedden, Michael Brooks, Jean Pitot, Elena Lopez, Martin Leary, Filippo Berto, and Anton du Plessis. Metal additive manufacturing in aerospace: A review. *Materials & Design*, 209:110008, 2021.
- [3] Ane Miren Mancisidor, Emma Gil, Fermin Garciandia, Maria San Sebastian, Oihan Lizaso, and Mauricio Escubi. Stirling engine regenerator based on lattice structures manufactured by selective laser melting. *Procedia CIRP*, 74:72–75, 2018.
- [4] Brandon J Walker, Benjamin L Cox, Ulas Cikla, Gabriel Meric de Bellefon, Behzad Rankouhi, Leo J Steiner, Puwadej Mahadumrongkul, George Petry, Mythili Thevama-

- ran, Rob Swader, et al. An investigation into the challenges of using metal additive manufacturing for the production of patient-specific aneurysm clips. *Journal of Medical Devices*, 13(3), 2019.
- [5] M Munsch. Laser additive manufacturing of customized prosthetics and implants for biomedical applications. In *Laser additive manufacturing*, pages 399–420. Elsevier, 2017.
 - [6] RCY Auyeung, H Kim, S Mathews, N Charipar, and A Piqué. Laser additive manufacturing of embedded electronics. In *Laser additive manufacturing*, pages 319–350. Elsevier, 2017.
 - [7] Jean-Pierre Kruth, Ludo Froyen, Jonas Van Vaerenbergh, Peter Mercelis, Marleen Rombouts, and Bert Lauwers. Selective laser melting of iron-based powder. *Journal of materials processing technology*, 149(1-3):616–622, 2004.
 - [8] YP Yang, M Jamshidinia, P Boulware, and SM Kelly. Prediction of microstructure, residual stress, and deformation in laser powder bed fusion process. *Computational Mechanics*, 61(5):599–615, 2018.
 - [9] Erik R Denlinger, Jarred C Heigel, Pan Michaleris, and TA Palmer. Effect of inter-layer dwell time on distortion and residual stress in additive manufacturing of titanium and nickel alloys. *Journal of Materials Processing Technology*, 215:123–131, 2015.
 - [10] Ankur Kumar Agrawal, Gabriel Meric de Bellefon, and Dan Thoma. High-throughput experimentation for microstructural design in additively manufactured 316l stainless steel. *Materials Science and Engineering: A*, 793:139841, 2020.
 - [11] Ala’aldin Alafaghani, Ala Qattawi, and Mauricio Alberto Garza Castañón. Effect of manufacturing parameters on the microstructure and mechanical properties of metal laser sintering parts of precipitate hardenable metals. *The International Journal of Advanced Manufacturing Technology*, 99(9):2491–2507, 2018.
 - [12] Hong Wu, Junye Ren, Qianli Huang, Xiongfei Zai, Ling Liu, Chao Chen, Shifeng Liu, Xin Yang, and Ruidi Li. Effect of laser parameters on microstructure, metallurgical defects and property of alsi10mg printed by selective laser melting. *Journal of Micromechanics and Molecular Physics*, 2(04):1750017, 2017.
 - [13] Zahabul Islam, Ankur Kumar Agrawal, Behzad Rankouhi, Collin Magnin, Mark H Anderson, Frank E Pfefferkorn, and Dan J Thoma. A high-throughput method to define additive manufacturing process parameters: Application to haynes 282. *Metallurgical and Materials Transactions A*, 53(1):250–263, 2022.
 - [14] Amal Charles, Ahmed Elkaseer, Lore Thijs, Veit Hagenmeyer, and Steffen Scholz. Effect of process parameters on the generated surface roughness of down-facing surfaces in selective laser melting. *Applied Sciences*, 9(6):1256, 2019.
 - [15] Yicha Zhang, Alain Bernard, Ramy Harik, and KP Karunakaran. Build orientation optimization for multi-part production in additive manufacturing. *Journal of Intelligent Manufacturing*, 28(6):1393–1407, 2017.

- [16] Erva Ulu, Nurcan Gecer Ulu, Walter Hsiao, and Saigopal Nelaturi. Manufacturability oriented model correction and build direction optimization for additive manufacturing. *Journal of Mechanical Design*, 142(6), 2020.
- [17] Marina A Matos, Ana Maria AC Rocha, and Ana I Pereira. Improving additive manufacturing performance by build orientation optimization. *The International Journal of Advanced Manufacturing Technology*, 107(5):1993–2005, 2020.
- [18] Luca Di Angelo, Paolo Di Stefano, and Emanuele Guardiani. Search for the optimal build direction in additive manufacturing technologies: a review. *Journal of Manufacturing and Materials Processing*, 4(3):71, 2020.
- [19] HD Morgan, JA Cherry, S Jonnalagadda, D Ewing, and J Sienz. Part orientation optimisation for the additive layer manufacture of metal components. *The International Journal of Advanced Manufacturing Technology*, 86(5):1679–1687, 2016.
- [20] Jennifer Bracken, Thomas Pomorski, Clinton Armstrong, Rohan Prabhu, Timothy W Simpson, Kathryn Jablokow, William Cleary, and Nicholas A Meisel. Design for metal powder bed fusion: the geometry for additive part selection (gaps) worksheet. *Additive Manufacturing*, 35:101163, 2020.
- [21] Ö Poyraz, E Yasa, G Akbulut, A Orhangül, and S Pilatin. Investigation of support structures for direct metal laser sintering (dmls) of in625 parts. In *2015 International Solid Freeform Fabrication Symposium*. University of Texas at Austin, 2015.
- [22] Jie Song, Youxiang Chew, Lishi Jiao, Xiling Yao, Seung Ki Moon, and Guijun Bi. Numerical study of temperature and cooling rate in selective laser melting with functionally graded support structures. *Additive Manufacturing*, 24:543–551, 2018.
- [23] Hyeyun Song, Tom McGaughy, Alber Sadek, and Wei Zhang. Effect of structural support on microstructure of nickel base superalloy fabricated by laser-powder bed fusion additive manufacturing. *Additive Manufacturing*, 26:30–40, 2019.
- [24] Tatiana Mishurova, Sandra Cabeza, Tobias Thiede, Naresh Nadammal, Arne Kromm, Manuela Klaus, Christoph Genzel, Christoph Haberland, and Giovanni Bruno. The influence of the support structure on residual stress and distortion in slm inconel 718 parts. *Metallurgical and materials transactions A*, 49(7):3038–3046, 2018.
- [25] Jingchao Jiang, Xun Xu, and Jonathan Stringer. Support structures for additive manufacturing: a review. *Journal of Manufacturing and Materials Processing*, 2(4):64, 2018.
- [26] Benjamin Blackford, Gene Zak, and Il Yong Kim. The effect of scan path on thermal gradient during selective laser melting. *The International Journal of Advanced Manufacturing Technology*, 110(5):1261–1274, 2020.
- [27] Paul A Hooper. Melt pool temperature and cooling rates in laser powder bed fusion. *Additive Manufacturing*, 22:548–559, 2018.

- [28] Koichi Masubuchi. *Analysis of welded structures: residual stresses, distortion, and their consequences*, volume 33. Elsevier, 2013.
- [29] Erik R Denlinger and Pan Michaleris. Mitigation of distortion in large additive manufacturing parts. *Proceedings of the Institution of Mechanical Engineers, Part B: Journal of Engineering Manufacture*, 231(6):983–993, 2017.
- [30] Max Biegler, Beatrix AM Elsner, Benjamin Graf, and Michael Rethmeier. Geometric distortion-compensation via transient numerical simulation for directed energy deposition additive manufacturing. *Science and Technology of Welding and Joining*, 25(6):468–475, 2020.
- [31] Shukri Afazov, Willem AD Denmark, Borja Lazaro Toralles, Adam Holloway, and Anas Yaghi. Distortion prediction and compensation in selective laser melting. *Additive Manufacturing*, 17:15–22, 2017.
- [32] Shukri Afazov, Annestacy Okioga, Adam Holloway, Willem Denmark, Andrew Triantaphyllou, Sean-Anthony Smith, and Liam Bradley-Smith. A methodology for precision additive manufacturing through compensation. *Precision Engineering*, 50:269–274, 2017.
- [33] Botao Zhang, Lun Li, and Sam Anand. Distortion prediction and nurbs based geometry compensation for reducing part errors in additive manufacturing. *Procedia Manufacturing*, 48:706–717, 2020.
- [34] Guido AO Adam and Detmar Zimmer. Design for additive manufacturing—element transitions and aggregated structures. *CIRP Journal of Manufacturing Science and Technology*, 7(1):20–28, 2014.
- [35] Yu-shuang Huo, Chang Hong, Huai-xue Li, and Peng Liu. Influence of different processing parameter on distortion and residual stress of inconel 718 alloys fabricated by selective laser melting (slm). *Materials Research*, 23, 2020.
- [36] T Mukherjee, V Manvatkar, A De, and T DebRoy. Mitigation of thermal distortion during additive manufacturing. *Scripta materialia*, 127:79–83, 2017.
- [37] K Dai and L Shaw. Distortion minimization of laser-processed components through control of laser scanning patterns. *Rapid Prototyping Journal*, 2002.
- [38] Damien Buchbinder, Wilhelm Meiners, Norbert Pirch, Konrad Wissenbach, and Johannes Schrage. Investigation on reducing distortion by preheating during manufacture of aluminum components using selective laser melting. *Journal of laser applications*, 26(1):012004, 2014.
- [39] Deqiao Xie, Fei Lv, Huixin Liang, Lida Shen, Zongjun Tian, Jianfeng Zhao, Yingdong Song, and Cijun Shuai. Towards a comprehensive understanding of distortion in additive manufacturing based on assumption of constraining force. *Virtual and Physical Prototyping*, 16(sup1):S85–S97, 2021.

- [40] Subodh C Subedi, Dan J Thoma, and Krishnan Suresh. Truss-type support structures for slm. In *2021 International Solid Freeform Fabrication Symposium*. University of Texas at Austin, 2021.
- [41] Andrew S Glassner. *An introduction to ray tracing*. Morgan Kaufmann, 1989.
- [42] Subodh C. Subedi, Ahmad Shahba, Mythili Thevamaran, Dan J. Thoma, and Krishnan Suresh. Towards the optimal design of support structures for laser powder bed fusion-based metal additive manufacturing via thermal equivalent static loads. *Additive Manufacturing*, page 102956, 2022.
- [43] Joaquim Ciurana, Luis Hernandez, and Jordi Delgado. Energy density analysis on single tracks formed by selective laser melting with cocrmo powder material. *The International Journal of Advanced Manufacturing Technology*, 68(5-8):1103–1110, 2013.
- [44] Umberto Scipioni Bertoli, Alexander J Wolfer, Manyalibo J Matthews, Jean-Pierre R Delplanque, and Julie M Schoenung. On the limitations of volumetric energy density as a design parameter for selective laser melting. *Materials & Design*, 113:331–340, 2017.
- [45] Nathan M Newmark. A method of computation for structural dynamics. *Journal of the engineering mechanics division*, 85(3):67–94, 1959.
- [46] Robert D Cook et al. *Concepts and applications of finite element analysis*. John wiley & sons, 2007.
- [47] Shiguang Deng and Krishnan Suresh. Stress constrained thermo-elastic topology optimization with varying temperature fields via augmented topological sensitivity based level-set. *Structural and Multidisciplinary Optimization*, 56(6):1413–1427, 2017.
- [48] Krister Svanberg. A globally convergent version of mma without linesearch. In *Proceedings of the first world congress of structural and multidisciplinary optimization*, volume 28, pages 9–16. Goslar, Germany, 1995.